

Deuterated methanol in the pre-stellar core L1544[★]

L. Bizzocchi^{1,2}, P. Caselli², S. Spezzano³, and E. Leonardo¹

¹ Centro de Astronomia e Astrofísica, Observatório Astronómico de Lisboa, Tapada da Ajuda, 1349-018 Lisboa (Portugal); e-mail: [bizzocchi,elle]@oal.ul.pt

² Centre for Astrochemical Studies, Max-Planck-Institut für Extraterrestrische Physik, Gießenbachstraße 1, 85748 Garching (Germany); e-mail: [caselli,bizzocchi]@mpe.mpg.de

³ I.Physikalisches Institut, Universität zu Köln Zùlpicherstraße 77, D-50937 Köln (Germany); e-mail: spezzano@ph1.uni-koeln.de

Preprint online version: May 18, 2018

ABSTRACT

Context. High methanol (CH₃OH) deuteration has been revealed in Class 0 protostars with the detection of singly, doubly, and even triply D-substituted forms. Methanol is believed to form during the pre-collapse phase *via* gas-grain chemistry and then eventually injected into the gas when the heating produced by the newly formed protostar sublimates the grain mantles. The molecular deuterium fraction of the warm gas is thus a relic of the cold pre-stellar era and provides hints of the past history of the protostars.

Aims. Pre-stellar cores represent the preceding stages in the process of star formation. We aim at measuring methanol deuteration in L1544, a prototypical dense and cold core on the verge of gravitational collapse. The aim is to probe the deuterium fractionation process while the “frozen” molecular reservoir is accumulated onto dust grains.

Methods. Using the IRAM 30 m telescope, we mapped the methanol emission in the pre-stellar core L1544 and observed singly deuterated methanol (CH₂DOH and CH₃OD) towards the dust peak of L1544. Non-LTE radiative transfer modelling was performed on three CH₃OH emissions lines at 96.7 GHz, using a Bonnor–Ebert sphere as a model for the source. We have also assumed a centrally decreasing abundance profile to take the molecule freeze-out in the inner core into account. The column density of CH₂DOH was derived assuming LTE excitation and optically thin emission.

Results. The CH₃OH emission has a highly asymmetric morphology, resembling a non-uniform ring surrounding the dust peak, where CO is mainly frozen onto dust grains. The observations provide an accurate measure of methanol deuteration in the cold pre-stellar gas. The derived abundance ratio is [CH₂DOH]/[CH₃OH] = 0.10 ± 0.03, which is significantly smaller than the ones found in low-mass Class 0 protostars and smaller than the deuterium fraction measured in other molecules towards L1544. The singly-deuterated form CH₃OD was not detected at 3σ sensitivity of 7 mK km s⁻¹, yielding a lower limit of [CH₂DOH]/[CH₃OD] ≥ 10, consistent with previous measurements toward Class 0 protostars.

Conclusions. The low deuterium fractionation observed in L1544 and the morphology of the CH₃OH emission suggest that we are mainly tracing the outer parts of the core, where CO just started to freeze-out onto dust grains.

Key words. ISM: clouds – molecules – individual object (L1544) – radio lines: ISM

1. Introduction

Deuterium is known to be ~ 10⁵ times less abundant than hydrogen in the Universe (Linsky 2003); nonetheless, high abundances of D-containing isotopologues are common findings in many interstellar environments (e.g., Ceccarelli 2002; Roueff & Gerin 2003). During the past couple of decades, observations have revealed large molecular deuteration in low-mass pre-stellar cores and Class 0 protostars, where singly, doubly, and — in some instances — triply deuterated molecules have been detected (see, e.g., Ceccarelli et al. 2007).

Methanol (CH₃OH) is one of the species that show the highest D-enhancements: together with ammonia (Lis et al. 2002; van der Tak et al. 2002), it is one of the two molecules for which a triply deuterated form has been observed. CD₃OH has been revealed in the low-mass protostar IRAS 16293–2422 (Parise et al. 2004), a source showing extreme deuterium enhancements. It is, however, not a pathological case, because Parise et al. (2006)

also found very high abundances of CH₂DOH and CHD₂OH in an extended sample of low-mass Class 0 protostars.

Theoretical and experimental studies predict that methanol is formed on the grain surface by subsequent additions of hydrogen to iced CO (Tielens & Hagen 1982; Watanabe & Kouchi 2002). This process is thought to take place during the cold and dense pre-collapse phase (e.g., Öberg et al. 2011). Later on, the molecule is released in the gas when the heating of newly formed protostar sublimates the ices mantles (Ceccarelli et al. 2001). Methanol deuteration is thus likely to be produced completely by active grain-surface chemistry, controlled by the atomic D content of the accreting gas. The high atomic D/H ratio required to account for the observed fractionation (0.1–0.2, Parise et al. 2002) has been explained by invoking an efficient transfer of atomic deuterium from the HD main reservoir *via* the intermediate H₂D⁺/D₂H⁺ ions (Roberts et al. 2003; Parise et al. 2006), which are very abundant in the CO-depleted pre-stellar gas (e.g., Caselli et al. 2003; Phillips & Vastel 2003; Vastel et al. 2004; Parise et al. 2011). Presently, all the measured methanol deuteration have been satisfactorily reproduced by the most recent coupled gas–grain models (Taquet et al. 2012; Aikawa et al. 2012),

[★] Based on observations carried out with the IRAM 30 m Telescope. IRAM is supported by INSU/CNRS (France), MPG (Germany), and IGN (Spain).

thus supporting the hypothesis that D-fractionation in methanol is a distinctive relic of the protostars' past history.

In this context, it is very interesting to study methanol deuteration in the pre-stellar gas. Starless cores represent the early stage of low-mass protostar evolution and offer the opportunity to probe the initial conditions in the process of star formation. These objects have a simple structure with no central heating source and little (thermal) turbulence, thus providing a favourable environment to study molecular deuteration. In particular, measuring deuterated methanol in pre-stellar cores yields a further test of the process responsible for the build-up of D-bearing isotopologue reservoir onto grain mantles.

A few studies of methanol in the pre-stellar gas have been reported so far. Earlier detections of the parent species were accomplished in TMC 1, TMC 1C, L134N (= L183), and B335 (Friberg et al. 1988; Takakuwa et al. 1998, 2000), and also in some translucent clouds by Turner (1998). Later on, CH₃OH was also observed in L1498 and L1517B by Tafalla et al. (2006) and, together with its deuterated variant CH₂DOH, in the shocked gas of the Class 0 L1157 source (Codella et al. 2012). Previous detections of deuterated methanol in a sample of pre-stellar cores were also reported in a summarised form by Bacmann et al. (2007), but a detailed analysis of these observations is actually missing.

In this paper we report on the observation of CH₂DOH towards the starless cloud L1544, thus providing an accurate assessment of the methanol deuteration in the cold pre-stellar gas. Multi-frequency analysis of the CH₃OH emission (including non-LTE modelling) is performed in order to derive a reliable value for the column density of the main isotopologue. We finally compare the obtained fractionation ratio with the results derived in Class 0 protostars and discuss the implications suggested by the predictions based on gas-grain chemical models.

2. Observations

The methanol data presented here have been collected using the IRAM 30 m antenna, located at Pico Veleta (Spain) during three observing sessions in 2012–2013. Single-pointing observations towards the L1544 dust emission peak, located at coordinates $\alpha(\text{J2000}) = 05^{\text{h}}04^{\text{m}}17.21^{\text{s}}$ and $\delta(\text{J2000}) = +25^{\circ}10'42.8''$ (Caselli et al. 2002a), were carried out in October 2012, April 2013, and October 2013. The 3 mm lines of CH₃OH were observed using several tunings of the EMIR E090 receiver while surveying various organic molecules in L1544 (Spezzano et al. 2013, 2014). We used the FTS backend in the “fine” configuration, resulting in 7.2 GHz of instantaneous bandwidth divided in four sub-bands with a final unsmoothed resolution of 50 kHz. The CH₂DOH transitions were only observed during the April 2013 observing block. The E090 and E150 receivers were tuned at 89.780 and 134.07 GHz, respectively, and the line signals were collected in the lower-inner (LI) sideband. As for CH₃OH, we used the FTS backend in the “fine” mode. Frequency-switching was adopted as observing mode using frequency throws of 3.9 MHz at 3 mm and 7.8 MHz at 2 mm. The telescope pointing was checked every two hours on nearby bright radio quasars and was found accurate to 3–4". Typical system temperatures were 85–130 K at 97 GHz and 170–220 K at 108 and 134 GHz. The observed spectra were then converted from the T_{A}^* to the T_{mb} temperature scale adopting B_{eff} and F_{eff} values taken from the IRAM documentation. The rest frequencies and other spectroscopic parameters of the observed methanol lines are reported in Table 1.

L1544 was mapped during the Autumn 2013 session. We performed a 3' × 3' on-the-fly (OTF) map centred on the source dust emission peak (see above). The reference position was set at (−180", 180") offset with respect to the map centre. Three methanol lines at 96.7 GHz were observed using two different E090 setups in the LI sideband and FTS in “fine” mode. The spectral axis was thus sampled with a 50 kHz channel spacing. The map area was swept during 4.5 hours of telescope time by moving the antenna along an orthogonal pattern of linear paths separated by 8" intervals, corresponding to roughly one third of the beam FWHM (25.4" at 96.7 GHz). The mapping was carried out in good weather conditions ($\tau \sim 0.03$) and a typical system temperature of $T_{\text{sys}} \approx 90$ K. The data processing was done using the GILDAS¹ software (Pety 2005).

Table 1. Spectroscopic parameters of the observed methanol lines. Data are taken from Xu & Lovas (1997) for CH₃OH, from Pearson et al. (2012) for CH₂DOH, and from Anderson et al. (1988) for CH₃OD

Line	Rest frequency (MHz)	E_u/k_b (K)	g_u^a	A (10^{-5} s^{-1})
CH ₃ OH				
$2_{0,2} - 1_{0,1}, A^+$	96741.375	6.96	5	0.3408
$2_{1,2} - 1_{1,1}, E_2$	96739.362	12.53 ^b	5	0.2558
$2_{0,2} - 1_{0,1}, E_1$	96744.550	20.08 ^b	5	0.3407
$0_{0,0} - 1_{1,1}, E_1 - E_2$	108893.963	13.12 ^b	1	1.471
CH ₂ DOH				
$2_{0,2} - 1_{0,1}, e_0$	89407.817	6.40	5	0.202
$3_{0,3} - 2_{0,2}, e_0$	134065.381	12.83	7	0.730
CH ₃ OD				
$1_{1,0} - 1_{0,1}, A^- - A^+$	133925.423	8.6	3	2.982

^a Rotational degeneracy.

^b Energy relative to the ground $0_{0,0}, A$ rotational state.

3. Results

3.1. Mapping of CH₃OH

Figure 1 shows the maps obtained for the CH₃OH $2_{0,2} - 1_{0,1}$ (A^+), $2_{1,2} - 1_{1,1}$ (E_2), and $2_{0,2} - 1_{0,1}$ (E_1) transitions. The last is appreciably weaker because it comes from a level of higher energy (see Table 1). The reference centre of the map is indicated and coincides with the maximum of the continuum 1.3 mm emission (Ward-Thompson et al. 1999).

In the right-hand panel of Figure 2, we plot a grid of spectra of the $2_{0,2} - 1_{0,1}$ (A^+) and $2_{1,2} - 1_{1,1}$ (E_2) CH₃OH lines. They were taken in nine positions separated by 30", as shown in the left-hand panel of the figure. Here, the grey scale represents the summed integrated intensity of the two lines, whereas the blue contours plot the 1.3 mm continuum emission map (Ward-Thompson et al. 1999) smoothed at 22". The lines peak strongly at the position 6, (0", 30"), whereas the corresponding signals are reduced by one-half at the position 5, which coincides with the map reference centre and is also very close to the maximum of the dust emission.

The CH₃OH emission thus differs from the dust continuum and presents a single peak offset to the north-east. A weak intensity enhancement located to the south-west is also discernible,

¹ See GILDAS home page at the URL: <http://www.iram.fr/IRAMFR/GILDAS>.

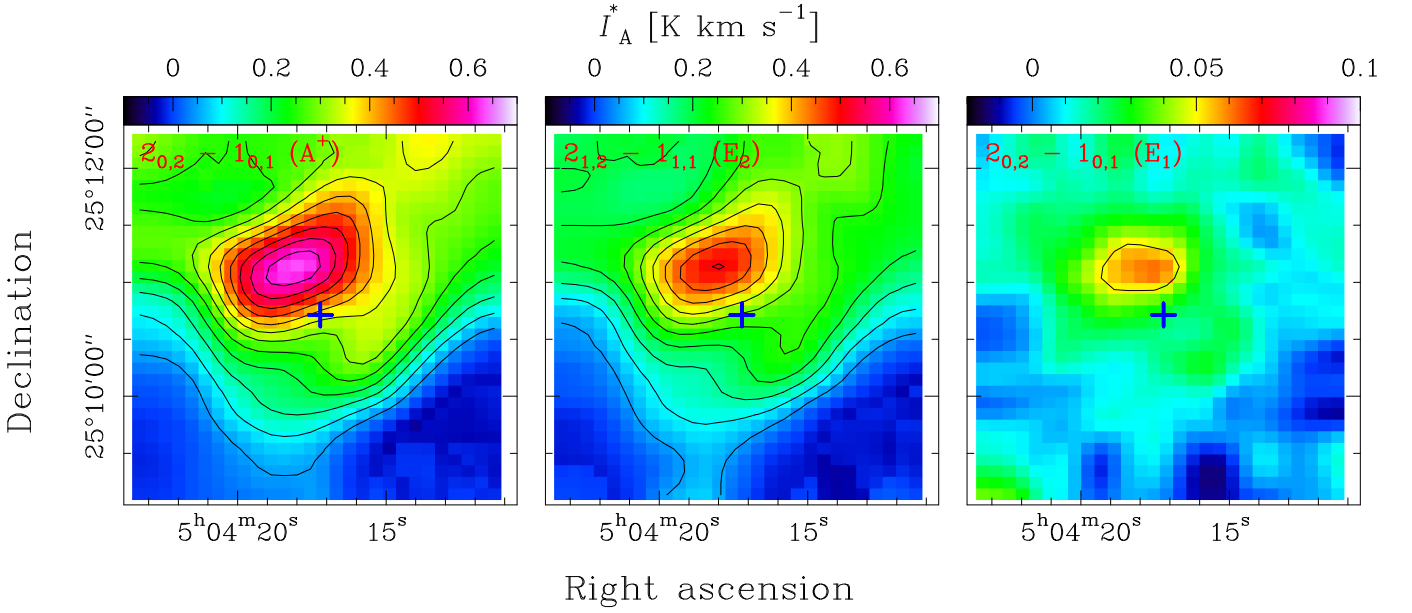


Fig. 1. Intensity maps (units of T_A^*) of the $2_{0,2} - 1_{0,1}$ (A^+), $2_{1,2} - 1_{1,1}$ (E_2), and $2_{0,2} - 1_{0,1}$ (E_1) transitions of CH₃OH integrated over 0.5 km s^{-1} velocity interval. The L1544 dust peak position located at $\alpha(\text{J2000}) = 05^{\text{h}}04^{\text{m}}17.21^{\text{s}}$, $\delta(\text{J2000}) = +25^{\circ}10'42.8''$ is indicated by the blue cross marker. The first contour is at 5σ and the increment is 5σ for all three maps; note however that the colour scale is different for the weak $2_{0,2} - 1_{0,1}$ (E_1) line (*right panel*). The images were smoothed to a $30''$ angular resolution to increase the signal-to-noise ratio ($1\sigma \approx 10^{-2} \text{ K km s}^{-1}$).

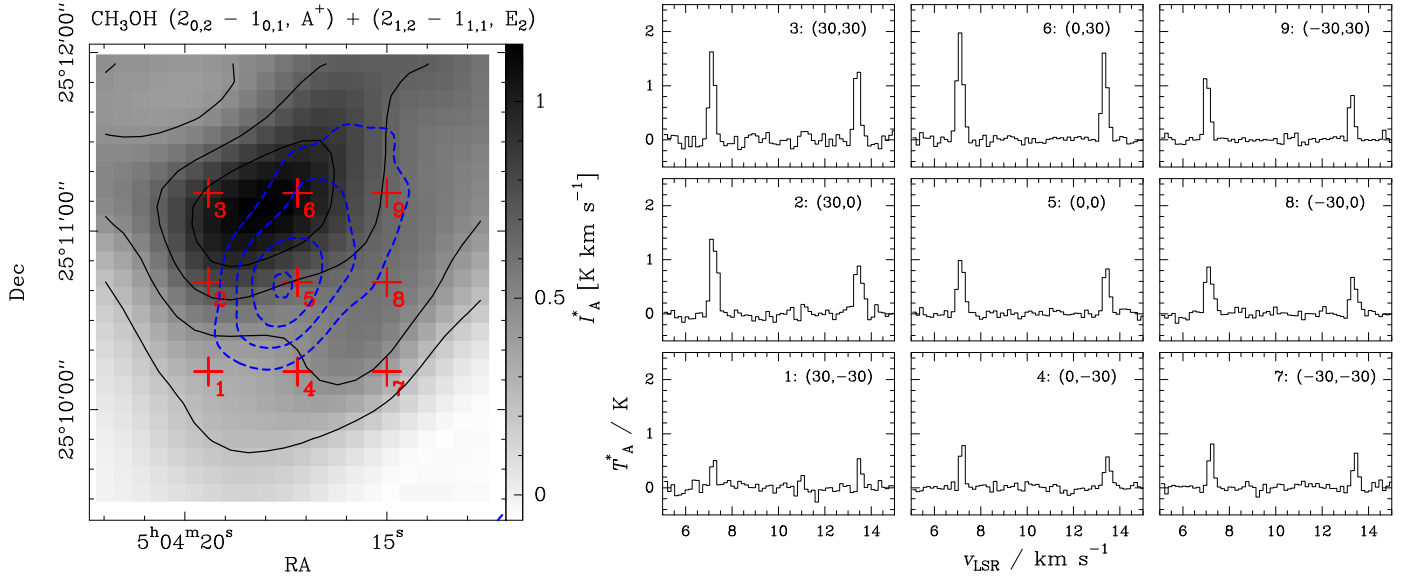


Fig. 2. (*Left panel*) Grey-scale map of the summed integrated intensity (units of T_A^*) of the $2_{0,2} - 1_{0,1}$ (A^+) and $2_{1,2} - 1_{1,1}$ (E_2) CH₃OH lines ($30''$ angular resolution). Five equally spaced contours from 0.23 to 1.5 K km s^{-1} are plotted. The blue dashed contours plot the 1.3 mm continuum intensity map of Ward-Thompson et al. (1999) smoothed at $22''$ to improve the signal-to-noise ratio. Contours are at 100 , 140 , 180 , and 220 mJy flux density levels. The red crosses represent the offset positions at which the spectra have been extracted. — (*Right panel*) Map spectra of the CH₃OH transitions towards the nine red crosses shown in the left panel. The velocity axis is centred on the $2_{0,2} - 1_{0,1}$ (A^+) line at 7.2 km s^{-1} . The vertical axis of each spectrum represents the T_A^* scale in K, as shown in the lower leftmost panel.

thus suggesting the presence of a highly asymmetrical broken ring distribution and reflecting the presence of a central CO depletion hole. This feature is apparent in the C¹⁷O integrated intensity map shown in Caselli et al. (1999) (see their figure 1). Also, the observed azimuthal asymmetry of the methanol emission is likely to be linked to slight inhomogeneities of the CO

depletion, owing to the non-spherical and cometary-shaped morphology (e.g., Tafalla et al. 2004; Crapsi et al. 2007).

3.2. CH₃OH single-pointing observations

Besides mapping, single-pointing, sensitive observations were performed towards the L1544 centre, corresponding to po-

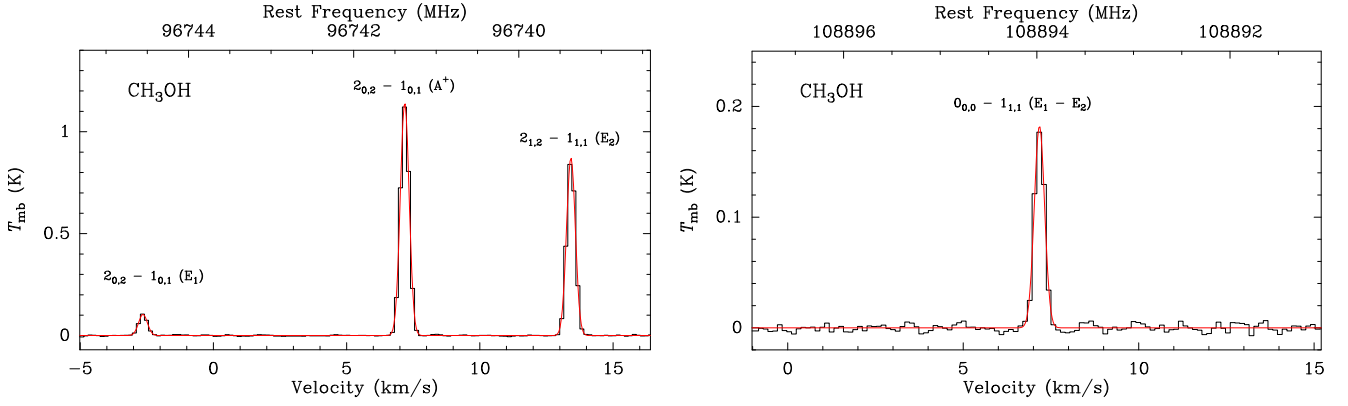


Fig. 3. CH₃OH lines observed towards the (0'',0'') position of L1544. (*left*) group of $2_{1,2} - 1_{1,1}$ and $2_{0,2} - 2_{0,1}$ transitions. — (*right*): $0_{0,0} - 1_{1,1}$ ($E_1 - E_2$) line. The spectral *rms* is ~ 3 mK. The red solid line plots the Gaussian fit obtained using CLASS.

sition 5 of Figure 2 (dust emission peak). Four CH₃OH emission lines were observed: three falling in a small frequency interval at 96.7 GHz (the same mapped, see Figure 1), plus one line at 108.9 GHz. The observations are shown in Figure 3. Line profiles were analysed using the GAUSS task of CLASS and the resulting data are reported in Table 2. The fit of the three closely spaced lines $2_{0,2} - 1_{0,1}$ (A^+), $2_{1,2} - 1_{1,1}$ (E_2), and $2_{0,2} - 1_{0,1}$ (E_1) was carried out by adjusting only one “common” line width. Given the relatively small number of channels used in the least-squares fit, the statistical error on the optimised parameters yielded by the GAUSS procedure could be optimistic. Thus, to be on the safe side, we conservatively quote 3σ uncertainties in Table 2.

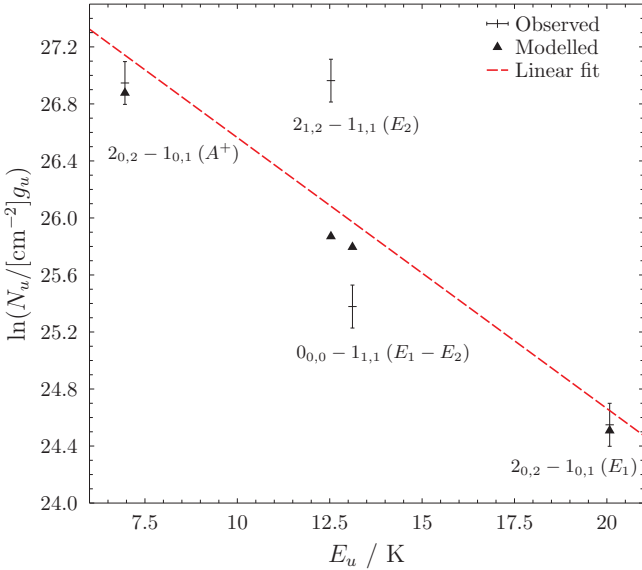


Fig. 4. Rotational diagram produced by the four CH₃OH lines observed towards L1544. A considerable scatter is apparent. The red dashed line represent the “best” linear fit of all data and yields $T_{\text{ex}} = 6 \pm 3$ K (see text).

The emitting levels have energies ranging from 7 to 20 K, thus one may try to derive the CH₃OH column density, N , and the average excitation temperature, T_{ex} , through the population diagram method (Goldsmith & Langer 1999). We used here the modified method described by Nummelin et al. (2000), which also includes the cosmic background emission and the peak optical depth in addition to T_{ex} and N . In this approach, the opti-

mised parameters were sought by minimising the squared sum of the error weighted differences between observed and modelled line intensities. These intensities are derived through the radiative transfer equality

$$T_{\text{mb}} = \eta_{\text{bf}} [J_{\nu}(T_{\text{ex}}) - J_{\nu}(T_{\text{bg}})] (1 - e^{-\tau_{\nu}}), \quad (1)$$

where η_{bf} is the source-beam filling factor, and $J_{\nu}(T)$ is the equivalent Rayleigh-Jeans temperature. Assuming a Gaussian line profile, the peak opacity of each transition is obtained as

$$\tau_{\nu}^{(\text{peak})} = \sqrt{\frac{\ln 2}{16\pi^3}} \frac{c^3 A g_u N}{v^3 Q(T_{\text{ex}}) \Delta v} e^{-E_u/kT_{\text{ex}}} (e^{h\nu/kT_{\text{ex}}} - 1). \quad (2)$$

Here, ν is the emission frequency, Δv the FWHM line width in units of velocity, E_u the energy of the upper level (as listed in Table 1), g_u the rotational degeneracy, A the Einstein’s coefficient for spontaneous emission, and $Q(T)$ is the rotation partition function at temperature T . This is computed by summing over all ($A + E$) rotational levels (Xu & Lovas 1997), whose energies are available at the CDMS² (Müller et al. 2005). Throughout the calculations, the average FWHM line width of 0.37 km s^{-1} was used and the beam filling factor η_{bf} was set to unity.

Table 2. Results of the CLASS GAUSS fit on the observed spectral profile of the methanol lines observed towards L1544. Numbers in parentheses refer to 3σ uncertainties in units of the last quoted digit.

Line	v_{LSR} (km s^{-1})	$\int T_{\text{A}}^* \nu$ (mK km s^{-1})	Δv (km s^{-1})
CH ₃ OH			
$2_{0,2} - 1_{0,1}$ (A^+)	7.1804(11)	472.4(25)	0.3888(12) ^a
$2_{1,2} - 1_{1,1}$ (E_2)	7.1808(14)	360.7(25)	0.3888(12) ^a
$2_{0,2} - 1_{0,1}$ (E_1)	7.194(11)	43.0(20)	0.3888(12) ^a
$0_{0,0} - 1_{1,1}$ ($E_1 - E_2$)	7.1723(78)	67.1(30)	0.346(17)
CH ₂ DOH			
$(2_{0,2} - 1_{0,1}, e_0)$	6.889(24)	30.5(42)	0.358(60)
$(3_{0,3} - 2_{0,2}, e_0)$	6.939(22)	31.3(45)	0.313(48)

^a Fitted as average value.

Once the best-fit N and T_{ex} are determined through Eqs. (1) and (2), the match between observed and modelled data can

² Cologne Databases for Molecular Spectroscopy, URL: <http://www.astro.uni-koeln.de/cdms/>

be presented in a population diagram fashion, $\ln(N_u/g_u)$ vs. E_u , where the N_u value for each transition is derived from the corresponding peak optical opacity through

$$N_u = [B_\nu(T_{\text{ex}}) - B_\nu(T_{\text{bg}})] \sqrt{\frac{4\pi^3}{\ln 2}} \frac{\tau_\nu^{(\text{peak})} \Delta\nu}{hcA}. \quad (3)$$

The result of this comparison is illustrated in Figure 4. The observed points exhibit a considerable scatter, largely exceeding the estimated error bars ($\sim 15\%$, including calibration and pointing uncertainties). The largest deviations are shown by the $2_{1,2} - 1_{1,1}$ (E_2) line, which appears substantially brighter than expected. The best-fit modelled points instead lie on a straight line, not far from the linear fit obtained under the assumptions of optically thin emission and negligible background radiation (Goldsmith & Langer 1999). Indeed, the derived peak optical depths are moderate ($\tau < 0.4$) and the cosmic background ($T_{\text{bg}} = 2.7$ K) emission merely acts as an offset. Figure 4 clearly indicates that excitation anomalies are present, thus preventing determination of a unique excitation temperature for all the rotational levels involved in the observed emissions. Indeed, the analysis yielded poorly constrained results: $T_{\text{ex}} = 6 \pm 3$ K and a column density value $N = (1.9 \pm 1.9) \times 10^{13} \text{ cm}^{-2}$.

3.3. Non-LTE modelling

To achieve a better constraint for the CH₃OH column density in L1544, we performed a non-LTE modelling using the radiative transfer code MOLLIE (Keto & Rybicki 2010) and the L1544 physical model with central density of $1 \times 10^7 \text{ cm}^{-3}$ described in Keto et al. (2014). The model is computed with a spherical Lagrangian hydrodynamic code with the gas temperature set by radiative equilibrium between heating by external starlight and cosmic rays and cooling by molecular line and dust radiation (see Keto & Caselli 2008 for a comprehensive discussion of the theory). Even if the L1544 emission maps show that the cloud is not spherical but instead has an elongated shape, the adopted model is simple, physically motivated and certainly adequate to model observation data averaged over a single dish beam profile. For the statistical equilibrium calculation, we used de-excitation rates for $p\text{-H}_2/A\text{-CH}_3\text{OH}$ and $p\text{-H}_2/E\text{-CH}_3\text{OH}$ collisional systems (Rabli & Flower 2010a) available at the LAMDA database (Schöier et al. 2005). Collisional data for

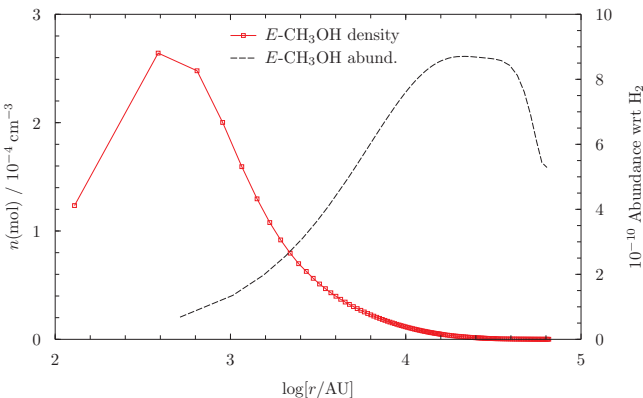


Fig. 5. (Left panel) Radial profiles for the $E\text{-CH}_3\text{OH}$ abundance (black) and density (red) corresponding to the best-fit input abundance of 9.2×10^{-10} . The radial trends were produced by the simple chemistry model implemented in the radiative transfer code MOLLIE (see text).

$o\text{-H}_2$ are lacking, but this does not represent a problem for our modelling because the H₂ *ortho-to-para* ratio (OPR) is expected to be very low in pre-stellar cores (see, e.g., Walmsley et al. 2004; Sipilä et al. 2013). Simulations were run separately for A and E symmetry species of methanol and considering only rotational levels below 36 K.

MOLLIE implements a simple CO chemistry (Keto & Caselli 2008) to take into account both the molecule freeze-out towards the inner cloud core and the photo-dissociation due to the UV stellar field at the edges. Since CO is considered to be the main precursors of methanol, we used the same model to describe the molecular abundance trend across the core. The “nominal” CH₃OH abundance, provided as the input parameter to MOLLIE, is thus internally translated in a radial abundance profile. As an example, the $E\text{-CH}_3\text{OH}$ radial abundance and density profile corresponding to the best-fit input abundance (see below) are illustrated in Figure 5. The resulting beam-averaged value of the CH₃OH column density (including both A and E species) is $2.66 \times 10^{13} \text{ cm}^{-2}$.

At the end of the computation, the code outputs a data cube representing the spectral distribution of the emerging radiation field. After convolution with the appropriate telescope beam ($25.5''$ at 97.6 GHz, $22.9''$ at 108.9 GHz), the modelled spectra were extracted from the central pixel and compared to the observations. Optimal χ^2 -fit between observed and modelled spectral

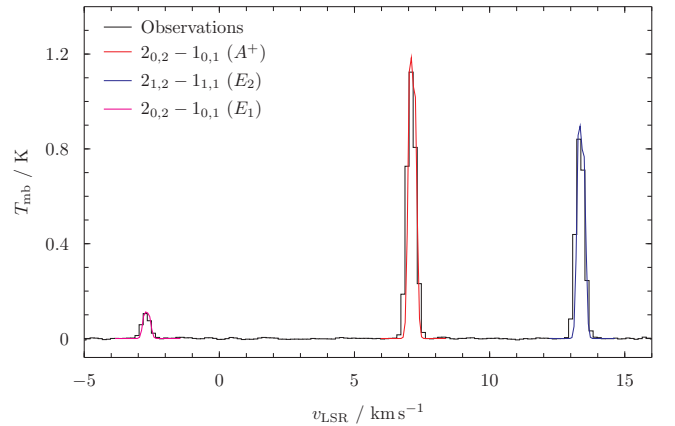


Fig. 6. Observed vs. modelled spectrum of CH₃OH in L1544. The black histogram shows the observations. Coloured lines indicate the best-fit modelled spectra. The velocity axis is centred on the $2_{0,2} - 1_{0,1}$ (A^+) line at 7.2 km s^{-1} .

profiles were found for the $2_{0,2} - 1_{0,1}$ (A^+), $2_{1,2} - 1_{1,1}$ (E_2), and $2_{0,2} - 1_{0,1}$ (E_1) transitions using input abundances of 9.5×10^{-10} and 9.2×10^{-10} , for A and E species, respectively. The modelling results for these three emissions falling at 96.7 GHz are shown in Figure 6.

Despite the success in reproducing these three lines, the fit underestimates the brightness of the observed $0_{0,0} - 1_{1,1}$ ($E_1 - E_2$) emission at 108.9 GHz by a factor of 4. Figure 7 illustrates the trend towards the excitation temperatures for the modelled $E\text{-CH}_3\text{OH}$ transitions as a function of the cloud radius. It shows that the $0_{0,0} - 1_{1,1}$ line is sub-thermally excited even at the high gas density of the cloud centre, where the other two E lines are instead thermalised. The reason for this behaviour is easily understood by inspecting Figure 8, which shows the bottom part of the rotational level diagram of $E\text{-CH}_3\text{OH}$, together with the radiative and collisional transitions considered in the present modelling. The $2_{0,2}$ and $2_{1,2}$ upper levels are connected to their corre-

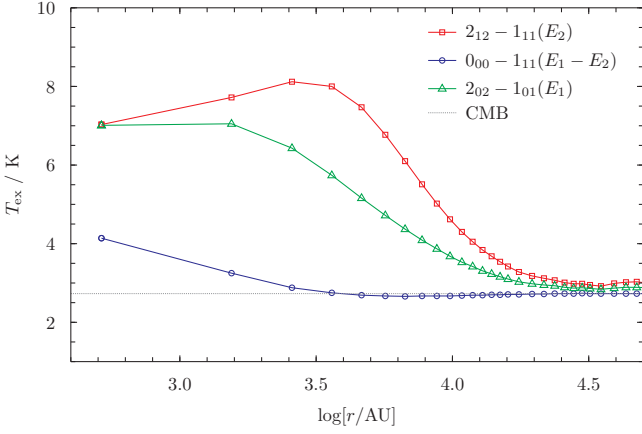


Fig. 7. Excitation temperature vs. cloud radius plot for the $2_{1,2} - 1_{1,1}$, $2_{0,2} - 1_{0,1}$, and $0_{0,0} - 1_{1,1}$ transitions of E -CH₃OH as computed by the present best-fit radiative transfer modelling.

sponding lower state within the $K_a = 0$ or $K_a = 1$ manifolds by “strong” collisional transitions (i.e., upward rate $> 10^{-11} \text{ cm}^3 \text{ s}^{-1}$ at 10 K), and other weaker $E_1 - E_2$ connections also exist. On the other hand, the collisional transitions connecting $0_{0,0}$ to the lower $1_{1,1}$ and $2_{1,2}$ states have rate coefficients that are set to zero in the present E -CH₃OH/ p -H₂ data set (Rabli & Flower 2010a). As discussed in Rabli & Flower (2010b), this is an artefact of the coupled state (CS) approximation used in the production of the collision cross sections, and it is very likely that the collisional $0_{0,0} - 1_{1,1}$ and $0_{0,0} - 2_{1,2}$ transitions actually have small, but non-zero, rate coefficients.

Repeated tests using altered sets of collisional data showed that rate coefficients as small as $3 \times 10^{-11} \text{ cm}^3 \text{ s}^{-1}$ (ca. one third of the $2_{1,2} - 1_{1,1}$ upward rate) allow for a satisfactory modelling of the $0_{0,0} - 1_{1,1}$ ($E_1 - E_2$) emission without significantly altering the fit quality of the $2_{1,2} - 1_{1,1}$ (E_2) and $2_{0,2} - 1_{0,1}$ (E_1) transitions. This finding thus suggests that the difficulties encountered in modelling the $0_{0,0} - 1_{1,1}$ ($E_1 - E_2$) line are indeed caused by small inaccuracies in the collisional dataset used.

An estimate of the error bar associated to the CH₃OH column density was obtained as in Bizzocchi et al. (2013). The Gaussian width of the χ^2 profile (plotted vs. the free parameter) is used to get an estimate of the uncertainty involved in the optimisation process ($\sim 19\%$). A further 10% error is added in quadrature to take the telescope calibration into account, yielding a final estimate of a 22% relative uncertainty. We thus ended with $N(\text{CH}_3\text{OH}) = (2.7 \pm 0.6) \times 10^{13} \text{ cm}^{-2}$. This value is not far from the uncertain results derived using an LTE approach in § 3.2, and it provides a more accurate constraint for the CH₃OH column density in L1544.

3.4. Singly deuterated methanol (CH₂DOH)

Two lines of CH₂DOH have been detected towards L1544, $2_{0,2} - 1_{0,1}$ and $3_{0,3} - 2_{0,2}$, at 98.4 and 134.1 GHz, respectively. Both are a -type transitions belonging to the lower e_0 torsional state (see Table 1). The observations are shown in Figure 9, and the results of the CLASS Gaussian fits are reported in the last two rows of Table 2. Interestingly, both CH₂DOH lines peak at a slightly bluer velocity compared to the ones of the parent species, which in turn are consistent with the systemic velocity of L1544 (7.2 km s^{-1} , Caselli et al. 2002a). The difference, ca. 0.3 km s^{-1} , is small but significant given the fit statistical errors ($< 0.003 \text{ km s}^{-1}$ for most lines) and the spectral channel spacing

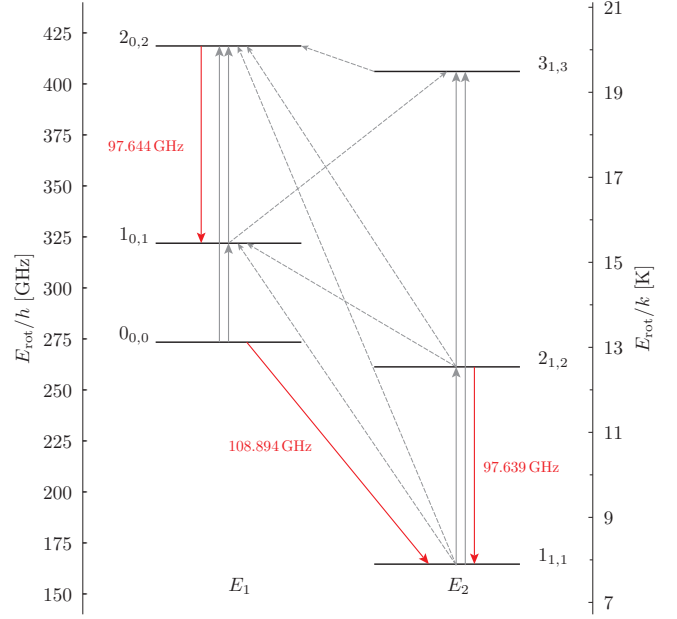


Fig. 8. Rotational energy plot for the lowest levels of E -CH₃OH. Active collisional channels are indicated by the upward grey arrows, with solid lines marking “strong” collisional transitions (upward rate $> 10^{-11} \text{ cm}^3 \text{ s}^{-1}$ at 10 K, Rabli & Flower 2010a). Red solid arrows indicate the *observed* radiative transitions.

of the observations ($0.11 - 0.15 \text{ km s}^{-1}$). It is also unlikely to be due to uncertainties in the rest frequencies because they are predicted to be as small as $\sim 0.005 \text{ km s}^{-1}$. The slight discrepancy is thus suggestive of a complex cloud dynamics, and it suggests that deuterated methanol traces a more confined (maybe inner) region with respect to its parent species. To confirm this, a map of CH₂DOH is required.

The CH₂DOH column density can be calculated from each transition assuming LTE conditions and optically thin emission once a suitable constraint for the excitation temperature, T_{ex} , is available. It holds that

$$N = \frac{8\pi\nu^3}{c^3} \frac{Q(T_{\text{ex}})}{g_u A_{ul}} \frac{e^{E_u/kT_{\text{ex}}}}{e^{h\nu/kT_{\text{ex}}} - 1} [J_\nu(T_{\text{ex}}) - J_\nu(T_{\text{bg}})]^{-1} \int T_{\text{mb}} d\nu. \quad (4)$$

Given the uncertainty of the excitation temperature determined for the parent species, the column density of the deuterated variant is derived through Eq. (4) assuming T_{ex} ranging between 5 and 8 K. The results are collected in Table 3.

Table 3. CH₂DOH column densities determined in L1544 assuming optically thin emission and excitation temperature in the 5–8 K interval.

	$N / 10^{12} \text{ cm}^{-2}$		
	$T_{\text{ex}} = 5 \text{ K}$	$T_{\text{ex}} = 6.5 \text{ K}$	$T_{\text{ex}} = 8 \text{ K}$
$Q(T)^a$	9.603	15.251	22.447
$2_{0,2} - 1_{0,1}$ (e_0)	2.11	2.14	2.43
$3_{0,3} - 2_{0,2}$ (e_0)	2.96	2.30	2.22

^a Rotational partition function.

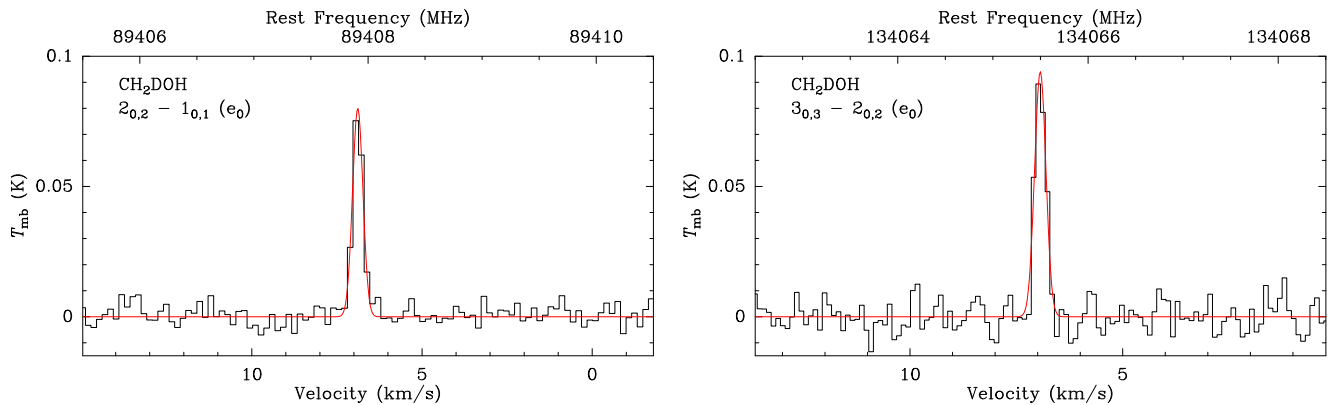


Fig. 9. CH₂DOH lines observed towards the (0'',0'') position of L1544. (*left*) $2_{0,2} - 1_{0,1} (e_0)$ — (*right*): $3_{0,3} - 2_{0,2} (e_0)$. The spectral rms is ~ 5 mK. The red solid line plots the Gaussian fit obtained using CLASS.

The rotational partition function, $Q(T)$ (whose values are also reported in Table 3) refers to the entire CH₂DOH population (i.e., it includes e_0 , e_1 , and o_1 levels) and was calculated by summing over rotational levels using the spectroscopic data of Pearson et al. (2012). The error bar of the CH₂DOH column density is estimated adding in quadrature the calibration error ($\sim 15\%$) and the maximum dispersion due to the uncertainty in T_{ex} . In this way we obtain $N(\text{CH}_2\text{DOH}) = (2.4 \pm 0.9) \times 10^{12} \text{ cm}^{-2}$.

We also performed sensitive observations at the frequency of the $1_{1,0} - 1_{0,1} (A^- - A^+)$ line of the singly deuterated CH₃OD isotopologue, but they resulted in a non-detection. The achieved 3σ sensitivity was 7 mK km s^{-1} (assuming a line width similar to that found for CH₂DOH) thus, with T_{ex} constrained in the 5–8 K interval, we derived a 3σ upper limit of $2.4 \times 10^{11} \text{ cm}^{-2}$ for the beam-averaged CH₃OD column density (see next section for a possible explanation of this non-detection).

4. Discussion and conclusion

We have detected two lines of CH₂DOH in L1544 and carried out an accurate evaluation of the methanol deuteration in a cold pre-stellar gas. From the beam-averaged column densities computed in § 3.3 and 3.4, we obtain a fractionation ratio $[\text{CH}_2\text{DOH}]/[\text{CH}_3\text{OH}] = 0.10 \pm 0.03$, a value significantly lower than the ones measured in low-mass Class 0 protostars (0.4–0.6, Parise et al. 2006), and lower than the deuterium fraction measured in molecules such as N₂H⁺, NH₃, and H₂CO (Caselli et al. 2002b; Bacmann et al. 2003; Roueff et al. 2005; Crapsi et al. 2007). However, it should be noted that, unlike methanol, all these molecules can also form in the gas phase, so that only our results reflect the surface chemistry activity directly.

State-of-the-art gas–grain chemical models of deuterium chemistry have been recently published by Aikawa et al. (2012) and Taquet et al. (2012). These studies follow the molecular evolution and the D-fractionation as star formation proceeds from the pre-collapse phase to a proto-stellar core. Both models are able to reproduce the high $[\text{CH}_2\text{DOH}]/[\text{CH}_3\text{OH}]$ ratio observed in Class 0 protostars if D and H abstraction and substitution are included in the chemical network. At densities of $5 \times 10^6 \text{ cm}^{-3}$ and $T = 10 \text{ K}$, the observed deuterium enhancement is reached in the molecular ice after $10^4 - 10^5 \text{ yr}$ (relatively faster, $\sim 5 \times 10^3 \text{ yr}$, following Taquet et al. calculations). On the other hand, a recent study of the gas-phase D-fractionation process (Kong et al. 2013) indicates that the gas within the inner core of L1544 has a deuteration age (estimated through N₂H⁺)

of five to eight times the free-fall time scale, which is of the order of 10^4 yr . This suggests that the deuterium reservoir frozen on grains should be fully developed, at least in the central region of the core.

However, it should be noted that the column densities have been derived from observations towards the core centre, where CH₃OH suffers a considerable depletion (see Figure 1). Thus, the present observations may mostly be sensitive to the outer parts of the core, where the deuterium fractionation is lower than in the region traced by N₂H⁺, a molecular ion not significantly depleted at high gas densities (e.g., Bizzocchi et al. 2013). The observed methanol deuteration is intermediate between the N₂D⁺/N₂H⁺ (0.2) and DCO⁺/HCO⁺ (0.04) found by Caselli et al. (2002b) in L1544. This gives the hint that methanol deuteration is indeed tracing the region where CO is freezing out (at densities of a few 10^4 cm^{-3}), where the D/H ratio is not high enough to reach D-fractions close to the ones found towards Class 0 sources or the centre of L1544. Inner regions are lost to view, since freeze-out is probably too efficient or because the product of deuteration remains on the grains, because centre grains are covered with N₂ towards the core (see, e.g., Bertin et al. 2013). Also, the morphology of the CH₂DOH emission in L1544 is not known, so the low measured $[\text{CH}_2\text{DOH}]/[\text{CH}_3\text{OH}]$ ratio might be produced by chemical inhomogeneities present in this pre-stellar core. Further progress in this study requires sensitive, interferometric observations aimed at deriving a detailed view of the fractionation in the different regions of the source.

From our non-LTE modelling results, we may infer that gas-phase CH₃OH in L1544 is composed of an almost equimolar mixture of *A* and *E* species, and the resulting $[E]/[A]$ ratio is 0.97 ± 0.26 . Given the large associated uncertainty, we may conclude that this value is consistent with the one implied by the picture of methanol formation on thermalised dust grains, (e.g., $[E]/[A] \approx 0.7$ at 10 K).

The singly-deuterated CH₃OD isotopologue was not detected by the present observations, yielding an upper limit of $2.4 \times 10^{11} \text{ cm}^{-2}$ for its column density. The corresponding ratio between the singly-deuterated forms of methanol is $[\text{CH}_2\text{DOH}]/[\text{CH}_3\text{OD}] \geq 10$, higher than the nominal value of 3 that is predicted on a statistical basis assuming that D atoms are randomly distributed in the methanol isotopologues (Rodgers & Charnley 2002). Our finding confirms the trend reported by Bacmann et al. (2007), and it agrees with the results of Class 0 protostars, where CH₃OD appears to be under-abundant with respect to the other methanol isotopic species

([CH₂DOH]/[CH₃OD] ~ 14–20, Parise et al. 2006). Also, large [CH₂DOH]/[CH₃OD] ratios have been found by Ratajczak et al. (2011) in a sample of low- to high-mass protostars.

The explanation of these “anomalous” ratios is still a challenge for the gas–grain chemical models, because H and D abstraction and substitution reactions — whose rates on ices are not very well constrained — are crucial to reproducing the observed abundances of the various methanol deuterated forms (e.g., Taquet et al. 2012). However, a laboratory study of low-temperature formaldehyde hydrogenation (Hidaka et al. 2009) shows that the formation of CH₂DOH in ice dominates CH₃OD, owing to the higher velocity of the H–D substitution process compared to the D-atom addition.

The CH₃OH emission has a highly asymmetric annular distribution surrounding the dust peak, where CO is mainly frozen onto dust grains. Methanol is expected to form via successive hydrogenation of CO on the surface of dust grains and then partially released in the gas phase upon formation (i.e., part of the formation energy is used to evaporate, in a process called reactive desorption; Garrod et al. 2006) and/or upon photo-desorption by UV photons produced by cosmic-ray impacts with H₂ molecules (Prasad & Tarafdar 1983). Evaporated methanol will then freeze-out onto dust grains in a time scale inversely proportional to the gas number density (~ 10⁹/n_H yr; van Dishoeck et al. 1993). Thus, the gas phase abundance of methanol is expected to decrease towards the centre of the core, where the density (and the freeze-out rate) is higher and where the outer layers of ice mantles may be rich in N₂, preventing hydrogenation of the underlying CO-rich layers (Bertin et al. 2013; Vasyunin & Herbst 2013).

Acknowledgements. We are grateful to the IRAM 30m staff for their support during the observations. L.B. and E.L. gratefully acknowledge support from the Science and Technology Foundation (FCT, Portugal) through the Fellowships SFRH/BPD/62966/2009 and SFRH/BPD/71278/2010. PC acknowledges the financial support of the European Research Council (ERC; project PALs 320620). L.B. also acknowledges travel support to Pico Veleta from TNA Radio Net project funded by the European Commission within the FP7 Programme.

References

- Aikawa, Y., Wakelam, V., Hersant, F., Garrod, R. T., & Herbst, E. 2012, *ApJ*, 760, 40
- Anderson, T., Crownover, R. L., Herbst, E., & De Lucia, F. C. 1988, *ApJS*, 67, 135
- Bacmann, A., Lefloch, B., Ceccarelli, C., et al. 2003, *ApJ*, 585, 55
- Bacmann, A., Lefloch, B., Parise, B., Ceccarelli, C., & Steinacker, J. 2007, in *Molecules in Space and Laboratory*
- Bertin, M., Fayolle, E. C., Romanzin, C., et al. 2013, *ApJ*, 779, 120
- Bizzocchi, L., Caselli, P., Leonardo, E., & Dore, L. 2013, *A&A*, 555, A109
- Caselli, P., van der Tak, F. F. S., Ceccarelli, C., & Bacmann, A. 2003, *A&A*, 403, L37
- Caselli, P., Walmsley, C. M., Tafalla, M., Dore, L., & Myers, P. C. 1999, *ApJ*, 523, L165
- Caselli, P., Walmsley, C. M., Zucconi, A., et al. 2002a, *ApJ*, 565, 331
- Caselli, P., Walmsley, C. M., Zucconi, A., et al. 2002b, *ApJ*, 565, 344
- Ceccarelli, C. 2002, *P&SS*, 50, 1267
- Ceccarelli, C., Caselli, P., Herbst, E., Tielens, A. G. G. M., & Caux, E. 2007, *Protostars and Planets V*, 47
- Ceccarelli, C., Loinard, L., Castets, A., et al. 2001, *A&A*, 372, 998
- Codella, C., Ceccarelli, C., Lefloch, B., et al. 2012, *ApJ*, 757, L9
- Crapsi, A., Caselli, P., Walmsley, M. C., & Tafalla, M. 2007, *A&A*, 470, 221
- Friberg, P., Hjalmarsen, A., Madden, S. C., & Irvine, W. M. 1988, *A&A*, 195, 281
- Garrod, R., Park, I. H., Caselli, P., & Herbst, E. 2006, *Faraday Discuss.*, 133, 51
- Goldsmith, P. F. & Langer, W. D. 1999, *ApJ*, 517, 209
- Hidaka, H., Watanabe, M., Kouchi, A., & Watanabe, N. 2009, *J. Phys. Conf. Series*, 194, 132024
- Keto, E. & Caselli, P. 2008, *ApJ*, 683, 238
- Keto, E., Rawlings, J., & Caselli, P. 2014, *MNRAS*, 440, 2616
- Keto, E. & Rybicki, G. 2010, *ApJ*, 716, 1315
- Kong, S., Caselli, P., Tan, J. C., & Wakelam, V. 2013, *ArXiv e-prints*, 1312.0971
- Linsky, J. L. 2003, *Space Sci. Rev.*, 106, 49
- Lis, D. C., Roueff, E., Gerin, M., et al. 2002, *ApJ*, 571, L55
- Müller, H. S. P., Schlöder, F., Stutzki, J., & Winnewisser, G. 2005, *J. Mol. Spectrosc.*, 242, 215
- Nummelin, A., Bergman, P., Hjalmarsen, Å., et al. 2000, *ApJS*, 128, 213
- Öberg, K. I., Boogert, A. C. A., Pontoppidan, K. M., et al. 2011, *ApJ*, 740, 109
- Parise, B., Belloche, A., Du, F., Güsten, R., & Menten, K. M. 2011, *A&A*, 526, A31
- Parise, B., Castets, A., Herbst, E., et al. 2004, *A&A*, 416, 159
- Parise, B., Ceccarelli, C., Tielens, A. G. G. M., et al. 2006, *A&A*, 453, 949
- Parise, B., Ceccarelli, C., Tielens, A. G. G. M., et al. 2002, *A&A*, 393, L49
- Pearson, J. C., Yu, S., & Drouin, B. J. 2012, *J. Mol. Spectrosc.*, 280, 119
- Pety, J. 2005, in *EdP-Sciences Conference Series*, ed. F. Casoli, T. Contini, J. Hameury, & L. Paganì, Vol. SF2A-2005, 721
- Phillips, T. G. & Vastel, C. 2003, in *SFChem 2002: Chemistry as a Diagnostic of Star Formation*, ed. C. L. Curry & M. Fich, 3
- Prasad, S. S. & Tarafdar, S. P. 1983, *ApJ*, 267, 603
- Rabli, D. & Flower, D. R. 2010a, *MNRAS*, 406, 95
- Rabli, D. & Flower, D. R. 2010b, *MNRAS*, 403, 2033
- Ratajczak, A., Taquet, V., Kahane, C., et al. 2011, *A&A*, 528, L13
- Roberts, H., Herbst, E., & Millar, T. J. 2003, *ApJ*, 591, L41
- Rodgers, S. D. & Charnley, S. B. 2002, *P&SS*, 50, 1125
- Roueff, E. & Gerin, M. 2003, *Space Sci. Rev.*, 106, 61
- Roueff, E., Lis, D. C., van der Tak, F. F. S., Gerin, M., & Goldsmith, P. F. 2005, *A&A*, 438, 585
- Schöier, F. L., van der Tak, F. F. S., van Dishoeck, E. F., & Black, J. H. 2005, *A&A*, 432, 369
- Sipilä, O., Caselli, P., & Harju, J. 2013, *A&A*, 554, A92
- Spezzano, S., Bizzocchi, L., Caselli, P., & Schlemmer, S. 2014, in prep.
- Spezzano, S., Brünken, S., Schilke, P., et al. 2013, *ApJ*, 769, L19
- Tafalla, M., Myers, P. C., Caselli, P., & Walmsley, C. M. 2004, *A&A*, 416, 191
- Tafalla, M., Santiago-García, J., Myers, P. C., et al. 2006, *A&A*, 455, 577
- Takakuwa, S., Mikami, H., & Saito, M. 1998, *ApJ*, 501, 723
- Takakuwa, S., Mikami, H., Saito, M., & Hirano, N. 2000, *ApJ*, 542, 367
- Taquet, V., Ceccarelli, C., & Kahane, C. 2012, *ApJ*, 748, L3
- Tielens, A. G. G. M. & Hagen, W. 1982, *A&A*, 114, 245
- Turner, B. E. 1998, *ApJ*, 501, 731
- van der Tak, F. F. S., Schilke, P., Müller, H. S. P., et al. 2002, *A&A*, 388, L53
- van Dishoeck, E. F., Blake, G. A., Draine, B. T., & Lunine, J. I. 1993, in *Protostar and planets III*, ed. V. Mannings, A. P. Boss, & S. S. Russell (University of Arizona Press), 163
- Vastel, C., Phillips, T. G., & Yoshida, H. 2004, *ApJ*, 606, L127
- Vasyunin, A. I. & Herbst, E. 2013, *ApJ*, 762, 86
- Walmsley, C. M., Flower, D. R., & Pineau des Forêts, G. 2004, *A&A*, 418, 1035
- Ward-Thompson, D., Motte, F., & André, P. 1999, *MNRAS*, 305, 143
- Watanabe, N. & Kouchi, A. 2002, *ApJ*, 571, L173
- Xu, L.-H. & Lovas, F. J. 1997, *J. Phys. Chem. Ref. Data*, 26, 17